Prefrontal working memory signal controls phase-coded information within extrastriate cortex

Mohsen Parto-Dezfouli[1,2*@], Isabel Vanegas[3*], Mohammad Zarei[4], William H. Nesse[3], Kelsey L. Clark[3], Behrad Noudoost[3,5@]

1 Max Planck Institute for Biological Cybernetics, 72076 Tübingen, Germany
2 Ernst Strüngmann Institute (ESI) for Neuroscience in Cooperation with Max Planck Society, 60528 Frankfurt, Germany
3 Department of Ophthalmology and Visual Sciences, John Moran Eye Center, University of Utah, Salt Lake City, UT, United States
4 Biosciences Institute, Newcastle University, Newcastle upon Tyne, UK
5 Lead

* Co-first author
@ Corresponding authors: mohsen.parto-dezfouli@esi-frankfurt.de, behrad.noudoost@utah.edu

Abstract

In order to understand how prefrontal cortex provides the benefits of working memory (WM) for visual processing we examined the influence of WM on the representation of visual signals in V4 neurons in two macaque monkeys. We found that WM induces strong β oscillations in V4 and that the timing of action potentials relative to this oscillation reflects sensory information- i.e., a phase coding of visual information. Pharmacologically inactivating the Frontal Eye Field part of prefrontal cortex, we confirmed the necessity of prefrontal signals for the WM-driven boost in phase coding of visual information. Indeed, changes in the average firing rate of V4 neurons were correlated with WM-induced oscillatory changes. We present a network model to describe how WM signals can recruit sensory areas by inducing oscillations within these areas and discuss the implications of these findings for a sensory recruitment theory of WM through coherence.

Keywords: neural phase code, working memory, top-down control, prefrontal cortex, neural oscillations

Introduction

Our capacity to dynamically interact with the world around us based on our own needs, priorities and goals is an example of our cognitive flexibility. The goals and plans preserved by working memory (WM) are capable of altering our perceptions of and actions toward the world around us. Thus, understanding how our plans alter the representation of sensory information can reveal the neural basis of cognitive flexibility. Prefrontal cortex (PFC) is believed to be one of the sources controlling sensory signals according to goals and plans[1-7]. In this study, we are specifically examining how WM information sent from PFC can influence the representation of sensory information in visual areas in macaque monkeys. We have already shown that the Frontal Eye Field (FEF) part of PFC sends a direct WM signal to extrastriate area V4[8], and visual areas manifest the WM content in their oscillatory behavior[9]. Within the FEF, WM alters the efficacy of V4 inputs as well, and these inputs mostly target neurons believed to be involved in the transformation of visual information into motor action[10]. The finding that extrastriate visual areas receive the content of WM, and that information sent from these areas to prefrontal cortex is undergoing a visuomotor transformation, provide a clear picture of the sequence of events giving rise to the benefits of WM. However, exactly how this top-down WM signal enhances the representation in visual areas is not known, considering that neurons in extrastriate visual areas show little or no change in their firing rate in response to WM content[11-15]. Thus, how WM impacts visual representations is crucial for understanding the neural code, since the behavioral consequences of WM[16-22] suggest that the representation altered by WM content is likely to be the representation that our behavior relies on.

Knowing that the FEF sends a spatially-specific signal to V4 carrying the content of WM[8], we studied the responses of V4 neurons while top-down WM is directed to their receptive field (RF) or elsewhere, under the conditions in which FEF activity is intact or disrupted using pharmacological manipulation. V4 neurons were provided with a bottom-up visual input with the goal of understanding how a top-down WM signal can alter the representation of bottom-up information. This arrangement revealed that WM primarily enhances the phase coding of visual information in V4. Pharmacological inactivation demonstrated that FEF activity is necessary for this phase-dependent representational enhancement in V4. We also show that average firing rate modulations within visual areas correlate with WM-induced oscillations within these areas, suggesting a possible role of WM-dependent oscillations in generating the other signatures of WM within sensory areas. These results support a WM model in which

sensory areas can potentially be recruited by higher areas without needing to change the average firing rate of sensory neurons.

Results

WM modulates oscillatory power and spike timing in V4, but not average firing rates

In order to assess the impact of WM on the visual representation, we recorded local field potentials (LFPs) and neuronal activity in extrastriate area V4 during a spatial WM task with visual signals presented to neurons independent of the WM demand (see Methods; Fig. 1A). The animal had to remember a visual cue presented either inside the V4 RF or in the opposite hemifield (memory IN and OUT conditions, respectively), and following a delay period, made a saccade to the remembered location to receive a reward. The background stimulus could have one of four orientations and three levels of contrasts (or no contrast, the classic memory-guided saccade (MGS) task), allowing us to examine the interaction between bottom-up sensory information and top-down WM signals. We recorded 145 V4 neurons across 88 recording sessions; most of our analysis focuses on their responses during the last 700ms of the delay period of the WM task.

As expected, V4 neurons were capable of signaling the properties of the background stimulus present in their RF. The left panel in figure 1B shows the response of a sample V4 neuron during the IN condition. During the fixation period and the cue period, the neuron exhibited sensitivity to different contrast levels of the background stimulus projected to its RF (main effect of contrast: $F_{Fixation}$=41.744, $p<10^{-16}$; F_{Cue}=14.541, $p<10^{-6}$; one-way ANOVAs). The neuron's contrast sensitivity was still manifested in its firing rate during the delay period (F_{IN}=19.950, $p<10^{-8}$; One-way). As shown on the right side of figure 1B, this neuron also showed contrast sensitivity during the delay period of the OUT condition (F_{OUT}= 17.851, $p<10^{-7}$; One-way ANOVA). Importantly, the contrast sensitivity during the delay period was not significantly different between the IN vs. OUT conditions ($F_{condition}$= $5x10^{-4}$, p=0.981; $F_{contrast}$=37.540, $p<10^{-16}$; $F_{interaction}$=0.301, p=0.742; Two-way ANOVA). Similarly, the neuron was selective for the orientation of the background stimulus. The neuron exhibited orientation sensitivity during the fixation period as well as the delay period in both IN and OUT conditions (main effect of orientation: $F_{Fixation}$=16.401, $p<10^{-8}$; F_{IN}=10.410, $p<10^{-5}$; F_{OUT}=19.014, $p<10^{-10}$; One-way ANOVAs; Fig. 1C). As with contrast, the content of WM (IN vs. OUT condition) did not significantly change the neuron's orientation sensitivity during the delay period ($F_{Condition}$= $5x10^{-4}$, p=0.982; $F_{Orientation}$=28.082, $p<10^{-16}$; $F_{Interaction}$=0.810, p=0.492; Two-way ANOVA). Thus,

this sample neuron exhibited contrast and orientation sensitivity for the background stimulus; however, WM did not alter the stimulus information reflected in the neuron's firing rate.

The same pattern was observed in the population of 145 V4 neurons: neurons' firing rates reflected the properties of the background stimulus, but this capacity was not affected by WM. The response to different background stimuli was similar between the fixation period, delay IN, and delay OUT conditions, both for contrast ($F_{Contrast}$=16.923, $p<10^{-7}$; $F_{Condition}$=0.311, p=0.733; $F_{Interaction}$=0.400, p=0.811; Two-way ANOVA) and orientation ($F_{Orientation}$=23.294, $p<10^{-14}$; $F_{Condition}$=0.770, p=0.465; $F_{Interaction}$=0.202, p=0.976; Two-way ANOVA) (Fig. 1D, 1E; see also Fig. S1A-B). Figure 1F shows the ability of V4 neurons to discriminate between all 12 stimuli of various contrasts and orientations across time. Overall, the ability of V4 neurons to discriminate between various background stimuli was not altered during the delay period of the IN vs. OUT conditions ($discriminability_{IN}$=1.514±0.783, $discriminability_{OUT}$=1.482±0.680, p=0.462; Fig. 1G; see also Fig. S1C-D). Therefore, whereas sensory information is reflected in the firing rate of V4 neurons, the impact of spatial WM on the sensory representation is not traceable by this neural signature.

In contrast to the lack of WM-driven change in firing rates, we found that V4 LFP oscillations strongly reflect the content of WM. WM-driven changes could be seen at the level of the average LFP (Fig. S2), and more robustly in the LFP power spectrum. Figure 1H shows the LFP power spectrum during the delay period for the same channel of recording as of the example neuron shown in figure 1B-C. The β (14-22 Hz; see Methods) band power was 0.019±0.013 dB/Hz during the IN condition, which is 18.9% greater than the 0.016±0.012 dB/Hz during the OUT condition (Wilcoxon ranksum, p=0.002). Therefore, although neurons' firing rates do not change due to WM, the power of the LFP oscillation in the β range reflects the impact of WM in the same recording channel. This phenomenon was observed across the 88 LFP recordings (Fig. 1I): β LFP power during the delay was greater for the IN condition compared to the OUT condition ($Power_{IN}$=2.001±0.336, $Power_{OUT}$=1.842±0.333, $p<10^{-3}$; Fig. 1J). Importantly, this WM-dependent enhancement of β power was observed independent of the background stimuli (Fig. S3); the discriminability based on the LFP power spectrum across frequencies is shown for different WM conditions in figure S4. In summary, a visual area known to receive the spatial WM signal exhibits the signature of this top-down signal in its subthreshold LFP activity, but not in neurons' firing rates.

The LFP reflects a combination of nearby currents, including synaptic inputs[23-26], and is not directly transmitted along axons to other brain areas in the manner that spikes are. Therefore, we sought to identify whether these WM-dependent oscillatory changes impact any other aspects of spiking activity

121 within V4. Although at the coarse scale of average firing rate there was no change due to WM, at a higher
122 temporal resolution it became evident that the timing of V4 action potentials depended on the phase of
123 WM-induced β oscillations. Figure 2A shows the distribution of spikes generated by a sample V4 neuron
124 across various phases of the β oscillation during the delay period, for memory IN and OUT conditions. The
125 average delay period FR was not different between the two memory conditions ($F_{Condition}$= 0.219, p=0.640;
126 $F_{Contrast}$=24.777, $p<10^{-10}$; $F_{Interaction}$=0.180, p=0.835; Two-way ANOVA), but the phase distribution of spikes
127 during the delay period of the IN condition was more concentrated (centered around 175-degree phase)
128 compared to the OUT condition. To quantify the phenomenon, we used the spike-phase locking (SPL) as a
129 measure of how consistently spikes of a neuron are generated at a certain phase. The SPL index varies
130 between 0 (spikes homogenously distributed across phases) to 1 (all spikes occurring at a certain phase).
131 For the sample neuron shown in figure 2A, SPL changed from 0.169 for the OUT to 0.189 for the IN
132 condition. Across the population of 145 V4 neurons, we found a consistent impact of WM on SPL: SPL
133 relative to the β oscillation was significantly greater during the IN condition compared to the OUT
134 condition (n=145 neurons; SPL_{IN}=0.164±0.014, SPL_{OUT}=0.155±0.005, $p<10^{-3}$; Fig. 2B). Conversely,
135 evaluating the consistency of the LFP at the time of V4 spikes, the spike triggered average (STA) LFP also
136 shows this strong coupling of spikes to LFP phase in the β range (Fig. S5). The 0% contrast condition,
137 equivalent to the classic MGS task, also showed significantly greater β power (n = 88 sessions;
138 $Power_{IN}$=1.957±0.0.651, $Power_{OUT}$=1.818±0.733, p=0.006, Wilcoxon signed-rank) and SPL (n=145 neurons,
139 SPL_{IN}=0.135±0.048, SPL_{OUT}=0.119±0.055, $p<10^{-7}$, Wilcoxon signed-rank) for the IN condition (Fig. S6); these
140 findings are similar to a previous report in visual area MT[9]. These results indicate that although WM does
141 not change the average firing rate, it influences V4 spike timing to be more closely aligned with WM-
142 dependent oscillations.

143 **Spatial WM specifically enhances phase coding of visual information**

144 To understand how WM-induced oscillations benefit the sensory representation within V4, we
145 examined whether V4 neurons' sensitivity was reflected in the timing of their spikes relative to these
146 WM-induced oscillations. As shown in figure 2C, analyzing the average normalized LFP at the time of
147 spiking (the STA) for an example neuron, we observed that in the presence of the high contrast stimulus in
148 the background during the memory IN condition, V4 spikes were associated with a steeper LFP change
149 compared to when a low contrast stimulus was in the background ($Slope_{High}$=0.052, $Slope_{Low}$=0.029). For
150 this neuron, this difference was less prominent during the OUT condition ($Slope_{High}$=0.042,

151 $Slope_{Low}$=0.035). We observed a similar phenomenon across the population. The LFP slope around the
152 time of a spike was significantly sharper when the preferred (high contrast) stimulus was presented in the
153 background, compared to the nonpreferred (low contrast) stimulus, during the IN condition
154 ($Slope_{High}$=0.047±0.002, $Slope_{Low}$=0.37±0.003, $p<10^{-3}$; Fig. 2D left). This difference was not observed during
155 the OUT condition ($Slope_{High}$=0.042±0.003, $Slope_{Low}$=0.036±0.003, p=0.686, Fig. 2D right). This indicates
156 that WM-induced oscillations can facilitate the spiking activity in visual areas, consistent with what other
157 groups have shown regarding the role of oscillations as a boost for passing the spiking threshold [27]. Similar
158 results were observed for preferred versus nonpreferred orientations (Fig. S7).

159 The idea that a WM-induced oscillation can change the timing of spikes also suggests the
160 possibility that the timing of spikes relative to that oscillation could convey information, referred to as a
161 neural phase code. We used the mutual information (MI) to quantify visual information conveyed by
162 either the phase or rate of spikes to have a side-by-side comparison of a neural phase vs. rate code (see
163 Methods). Figure 2E left shows the average population MI measured based on phase coding across time
164 for both the IN and OUT conditions. The presence of the WM cue reduced both phase and rate coding of
165 background information during the visual period (Phase MI_{IN}=0.007±0.001 bits, Phase MI_{OUT}=0.014±0.002
166 bits; p=0.012; Rate MI_{IN}=0.019±0.002 bits, Rate MI_{OUT}=0.031±0.003 bits; p=0.012). However, maintenance
167 of WM information during the delay period increased the phase coding capacity of the V4 neurons to
168 represent information about the stimulus in their RF, but did not alter their rate coding. Figure 2F shows
169 the capacity of V4 neurons to encode the background stimulus during the IN vs. OUT conditions under
170 phase (left) and rate (right) coding schemes. Phase MI during the delay period of the IN condition was
171 0.019±0.002 bits, significantly greater than the 0.012±0.002 bits during the OUT condition ($p<10^{-3}$).
172 However, delay period rate MI was not significantly different between the IN and OUT conditions
173 (MI_{IN}=0.024±0.003 bits; MI_{OUT}=0.022±0.003 bits, p=0.261). We also found that the WM-dependent
174 enhancement of phase-dependent visual representation was limited to the β range oscillations (Fig. 2G) It
175 is imperative to note that despite the seemingly small values of MI (e.g., 0.019 bits), an increase of 54% in
176 phase MI between the IN and OUT conditions means a huge boost in coding capacity due to WM. The MI
177 value can be interpreted as a measure of the rate of statistical learning from incoming data through which
178 sensory decisions can be made. For example, with 0.012 bits per 100 ms phase MI available in the OUT
179 condition, for a population of 100 neurons firing independently it would take 294 ms to fully differentiate
180 12 stimuli. WM-induced enhancement of phase MI means that the same discriminatory capacity can be
181 achieved within 190 ms with the same number of neurons, or within the same amount of time but with

182 only 65 neurons. Altogether, consistent with the finding that WM mainly modulated oscillations within
183 the β range (Fig. 1I, J), we found that WM mostly improves the phase coding in V4 within the same β
184 range. Thus, WM specifically enhanced β range phase coding in V4, without altering rate coding.

185

186 **FEF activity is necessary for the phase-dependent representation within V4 during WM.**

187 FEF sends direct projections to V4; these projections arise primarily in the superficial layers of FEF
188 [28-30], and are functionally characterized by delay activity reflecting the content of spatial WM[8]. To causally
189 test whether the observed WM-driven phase coding in V4 depended on signals received from the FEF, we
190 recorded from V4 neurons before and after pharmacologically inactivating a portion of the FEF using a
191 small-volume injection of the GABAa-agonist muscimol (Fig. 3A). Localized FEF inactivation is known to
192 impair performance on the MGS task in a spatially-specific manner[31,32]. As shown for an example
193 inactivation session in figure 3B: prior to inactivation, the animal performed well at all locations, and after
194 FEF inactivation performance was disrupted for conditions in which the cue appeared in the left hemifield,
195 contralateral to the inactivated FEF. Figure 3C shows average MGS performance over time at various
196 locations across 33 inactivation sessions: performance for the IN condition and neighboring locations
197 decreased over time following FEF inactivation. For the IN condition, the performance dropped from
198 90.32±2.62 percent correct before to 68.49±5.39 percent correct three hours after inactivation ($p<10^{-3}$).
199 Across the same 33 sessions, saccade error during the IN condition compared to the OUT condition was
200 not different prior to FEF inactivation ($Error_{IN}$=1.012±0.022, $Error_{OUT}$=0.989±0.023, p=0.520; Fig. 3D), but
201 was significantly greater for the IN condition after FEF inactivation ($Error_{IN}$=1.192±0.042,
202 $Error_{OUT}$=1.033±0.032, p=0.001; Fig. 3D). Similarly, reaction time (RT) increased following FEF inactivation
203 for the IN condition compared to the OUT condition (before inactivation: RT_{IN}=1.015±0.003,
204 RT_{OUT}=1.023±0.007, p=0.741; after inactivation: RT_{IN}=1.075±0.015, RT_{OUT}=1.014±0.006, $p<10^{-4}$, Fig. 3E).
205 We found no effect of the background stimulus on the task performance, either in terms of reaction time
206 (Fig. S8A; ANOVA between three contrasts: F_{IN}=1.75, p=0.180; ANOVA between four orientations:
207 F_{IN}=2.26, p=0.085) or in percent correct (Fig. S8B; ANOVA between three contrasts: F_{IN}=0.01, p=0.990;
208 ANOVA between four orientations: F_{IN}=0.06, p=0.979).

209 Next we evaluated the impact of FEF inactivation on V4 activity during WM. We recorded from 66
210 V4 neurons before and after FEF inactivation. Discriminability of the background stimulus based on V4
211 firing rates was unaltered, and based on LFP only slightly altered, following FEF inactivation (Fig. S9A-C).

212 Both the V4 LFP power spectrum and SPL showed a reduction in the β range following FEF inactivation
213 (Fig. S10). In these 66 neurons, prior to inactivation, the impact of WM on phase coding was evident:
214 during the delay period there was significantly stronger phase coding of information in the β range for the
215 memory IN condition (Fig. 2E-G; Phase MI_{IN}=0.023±0.004 bits, Phase MI_{OUT}=0.018±0.003 bits, p=0.039).
216 Consistent with figure 2E, WM did not alter the strength of rate coding (Rate MI_{IN}=0.022±0.005 bits, Rate
217 MI_{OUT}=0.020±0.005 bits, p=0.446). Importantly, the phase coded information within the β range during
218 the delay period of the task dropped following FEF inactivation (Fig. 3F). Figure 3G shows the cross section
219 of figure 3F at the β frequency, depicting the dynamics of phase MI over the course of a trial before and
220 after FEF inactivation. The MI values for individual neurons during the delay period of the IN condition for
221 each session are shown in figure 3H; following FEF inactivation, phase-coded MI in the β range dropped
222 from 0.023±0.004 bits to 0.014±0.003 bits (n= 66 neurons, p=0.005; Fig. 3H). The phase coded information
223 within the β range during the delay period of the task does not change following FEF inactivation for the
224 OUT condition (n= 66 neurons, p=0.281; Fig. S11). Rate coding, in contrast, was unaffected by FEF
225 inactivation (IN condition: Rate MI_{Pre}=0.022±0.005 bits, Rate MI_{Post}0.020±0.004 bits, p=0.880). Thus, WM's
226 enhancement of phase coding in V4 depended on activity within the FEF.

227

228 **Modelling WM-driven changes in phase and rate coding**

229 The finding that WM mainly modulates phase coded information within extrastriate areas
230 fundamentally shifts our understanding of how the top-down influence of prefrontal cortex shapes the
231 neural representation, suggesting that inducing oscillations could be the main way WM recruits sensory
232 areas. However, while this side-by-side comparison of rate and phase coding shows the strength of the
233 latter, several studies have reported an impact of WM on the firing rate of visual neurons[8,15,33-35]. One can
234 argue that a slight increase in firing rate at each stage of visual processing can gradually accumulate to
235 eventually emerge in the form of a robust firing rate change[12], and that this will be sufficient to support
236 WM. In order to determine the primary means by which WM alters neural representations, we
237 constructed a neural field network model of visual areas during WM. In order to examine the impact of
238 WM on oscillatory and firing rate changes in visual areas, we designed the model to consist of
239 interconnected excitatory and inhibitory units (Fig. 4A, e-cells and i-cells) capable of generating oscillatory
240 activity. To modulate this oscillatory activity, these neural field units received bottom-up and top-down
241 type input. The units were tuned to different stimulus 'features' of the bottom-up input (analogous to

242 orientation tuning of V4 neurons in the experimental data, with input strength analogous to contrast).
243 The top-down input was not feature selective, providing a uniform input across the network, with
244 stronger connections to e-cells than i-cells, consistent with what is known about the FEF-V4 circuitry and
245 anatomy[8,36]. A higher strength of WM signal in the model corresponds to the memory IN condition, in
246 comparison to the absence of WM input in the memory OUT equivalent. The model replicates several key
247 features of the experimental data: units reflect sensory information in their phase and rate, WM-
248 enhanced β power, and locking of units' activity to this oscillation under the influence of WM (Fig. S12).
249 The model's phase coding of visual stimuli is evident in the relative timing of responses of differently
250 tuned e-cells to an input stimulus (Fig. 4B). Using this model, we can directly compare the magnitude of
251 information encoded by the phase and rate of model units, quantified via information gain (see Methods).
252 We found that not only was information encoded by phase much greater than that encoded by rate, but
253 also that phase and rate information were oppositely affected by changes in WM strength: phase
254 information increased and rate information decreased as the WM signal increased (Fig. 4C). We also
255 found this same divergent pattern between phase and rate codes when measuring coding performance
256 using mutual information (see Fig. S13). Therefore, the quantification of information within a tangible
257 network model revealed that in an oscillating network, a top-down induced oscillation can be detrimental
258 to the rate-dependent representation of information.

259 The model revealed that stronger WM input increased both oscillation strength and peak
260 frequency (Fig. S12), and we hypothesized that this change in frequency could explain changes in firing
261 rate. We tested this idea both in the model and in the experimental data. In the model, we varied the
262 strength of the WM signal across 4 levels of stimulus input strength (resembling various levels of stimulus
263 contrast). We then divided oscillatory cycles occurring in the respective stimulus input levels into deciles
264 based on their oscillation frequency, and measured information encoded by phase and rate as a function
265 of oscillation frequency (Fig. 4D). Phase information increased with increasing oscillation frequency while
266 rate information decreased at higher oscillation frequencies, for all non-zero contrast levels (Model utility
267 t-test for contrasts 0-3 respectively; phase code: $p>0.05$, >0.05, <0.01,0.001; and rate code: $p>0.05$,
268 <0.05,0.01,0.0001). Importantly, we found that the network replicating the oscillatory and
269 representational characteristics of V4 during WM shows an increased firing rate as oscillation frequency
270 increases. Figure 4E shows how small variations in the strength of the WM signal resulted in correlated
271 changes in oscillation frequency and firing rate ($r = 0.901$; linear model utility t-test significant: $p<0.0001$).
272 Thus, firing rate is positively correlated with oscillation frequency, but information encoded by that rate is

negatively correlated (Fig. 4C vs. 4E). To confirm that such a relationship exists in the experimental data, for each neuron we measured the peak LFP frequency and average firing rate across subsamples of trials, allowing us to test the relationship between peak β frequency and evoked firing rate within a single condition. As shown for two sample V4 neurons, such a relationship between peak frequency and average firing rate existed between the IN and OUT conditions (for a single background stimulus; Fig. 4F). For the first sample neuron, in which the peak frequency changed from 18.81 to 15.84 Hz between the IN and OUT conditions, the firing rate changed from 1.084 to 0.869, and peak frequency and firing rate were correlated across subsamples of trials (Pearson correlation, $r=0.716$, $p<10^{-32}$; Fig. 4F left). Results from the second sample neuron show that this relationship remains the same even in cases where WM reduces the peak frequency (peak-frequency$_{IN}$ = 15.041 Hz, peak-frequency$_{OUT}$ = 16.827 Hz, $FR_{IN}=0.630$, $FR_{OUT}=0.816$): the correlation between firing rate and peak frequency remains positive (Pearson correlation, $r=0.671$, $p<10^{-26}$; Fig. 4F right). At the population level, we looked at firing rate during the delay period across subsamples of trials for all 145 V4 neurons, sorted according to their peak frequency (Fig. 4G). As shown in figure 4G left, this relationship between peak frequency and firing rate was present across both IN and OUT conditions; more importantly, this relationship remained the same between the two memory conditions ($F_{Condition}=9.649$, $p=0.003$; $F_{Frequency}=399.566$, $p<10^{-31}$; $F_{Interaction}=2.935$, $p=0.091$, ANCOVA), suggesting that the frequency of WM-induced oscillations could account for firing rate changes. Critically, a similar analysis for the visual period of the task revealed that the presence or absence of a visual stimulus (IN vs. OUT condition) creates a much larger change in firing rate, which cannot be accounted for by changes in β frequency ($F_{Condition}=5.113\times10^{3}$, $p<10^{-72}$; $F_{Frequency}=103.220$, $p<10^{-15}$; $F_{Interaction}=71.427$, $p<10^{-11}$, ANCOVA) (Fig. 4G right). This relationship between frequency and firing rate was also significant within each contrast level (Fig. S14). In other words, changes in rate during the delay period may be a consequence of changes in phase locking frequency (although we cannot rule out that the firing rate is driving the frequency instead, or that changes in both rate and frequency are independently generated by a common input). We also examined the relationship between peak frequency and firing rate as a function of stimulus efficacy. Both firing rate and peak frequency vary with stimulus efficacy (Fig. S15A; two sample neurons), but there was no difference for this relationship between the IN and OUT condition (Fig. S15B). Figure S16 shows that this relationship between firing rate and peak frequency is specific to the β frequency range. While there was no overall change in average firing rate due to WM across the V4 population (see Fig. 1, Fig. S1, and related statistics), this analysis further suggests that any WM-related changes in the firing rates of individual V4 neurons could be driven by changes in oscillatory frequency.

Discussion

Prefrontal cortex modulates sensory and motor signals in order to guide our actions based on goals and priorities maintained in WM[3,4,37,38]. Within prefrontal areas, FEF sends direct projections to extrastriate visual areas, and activity in these projections reflects the content of WM[8]. We designed a paradigm in which neurons in extrastriate area V4 are provided with bottom-up input while the top-down signal carrying WM content can be directed to the part of space represented by these neurons or elsewhere. This allowed us to examine which aspect of the sensory representation within V4 is influenced by a top-down WM signal, and to causally test the role of FEF activity in this WM-driven modulation. We found that a neural phase code representation of sensory stimuli was strongly modulated by top-down WM signals coming from the FEF, while firing rates were relatively unaffected, suggesting that representations based on the average firing rate of neurons might not be the primary way that top-down signals enhance sensory processing. Using a combination of computational modelling and experimental data analysis, we provided evidence that any changes in the average firing rate of individual neurons might be a byproduct of small changes in the frequency of the WM-induced oscillation.

Attention and WM are closely linked, although the exact nature of their relationship is not yet known [39-44]. Behaviorally, WM can impact sensory processing, changing discrimination thresholds [45-47] and reducing reaction times [48], similar to the behavioral effects of attention. In visual areas, spatial attention and WM have several similar impacts on visual responses: shifts in RFs[8,49,50], enhanced firing rates[8,51], decreased variability[8,52], and changes in inter-neuronal correlations[53,54]. Within FEF, neurons with WM-related activity show greater attentional modulation [55], and the same neurons in lateral PFC are involved in selection when switching between attention and WM tasks [56]. Although behavioral training can dissociate the neural basis of WM and attention in prefrontal cortex [57,58], it remains likely that by default these mechanisms are linked or overlapping. We cannot rule out the possibility that the animal is allocating attention to the WM location, and that this drives the phase coding; however, the feature information we see enhanced is task-irrelevant, has no measurable impact on performance, and the monkey hasn't been rewarded for attending to it. In the opposite direction, the task irrelevance of the stimuli may discourage attention, and this may be related to the lack of firing rate modulation. Additionally, our task involves a saccade to the remembered location. Motor planning also produces changes in visual cortex similar to those seen during attention [59]. All three of these processes—attention, motor planning, and WM—are heavily interconnected both behaviorally and neurally [60], and cannot be fully dissociated in our dataset. To our knowledge, no studies have reported on whether or not phase coding of visual information is

335 modulated by either covert spatial attention or motor preparation; further work will be needed to
336 determine whether the phase coding we report here is specific to WM or shared with covert attention
337 and/or motor planning.

338 The long[61] and growing[62-64] list of neural signatures of attention begs a unifying theory describing
339 the exact mechanisms involved in generating this plethora of neural signatures. Many of these signatures
340 are seen in both attention and WM, including enhanced visual responses[8,51], changes in inter-neuronal
341 correlations[53,54], decreased variability[8,52], and shifts in RFs[8,49,50]. In light of the present findings, we suggest
342 that by inducing an oscillation, top-down signals allow expression of sensory representations in the form
343 of a neural phase code: neurons emit action potentials in response to this induced oscillation with a
344 relative timing that reflects their sensitivity. Slight changes in the frequency of the oscillation might then
345 account for changes in the average firing rate of neurons in sensory areas, and one can imagine coherent
346 oscillations altering the dependent and independent variability of the neurons as well. Understanding
347 whether the β oscillations observed in our study function in the same way as the mostly gamma
348 oscillations reported in attention studies will require a more complete understanding of the
349 characteristics of oscillators operating in the presence and absence of visual information (see also [53]).

350 A framework in which top-down signals primarily alter the phase of the spikes faces an important
351 challenge: in communication between brain areas, LFP oscillations are not carried along with spikes down
352 axonal projections. A phase code without its oscillatory reference frame is likely unreadable. However,
353 studies in our lab and others have provided growing evidence that there are coherent oscillations
354 between brain areas during WM, which could provide the shared oscillatory frame of reference required
355 to transfer phase-coded information. For example, oscillatory coherence between FEF and inferotemporal
356 cortex exists and predicts performance on an object WM task[65]; similarly, synchrony between PFC and V4
357 is also correlated with WM performance[66]. Oscillatory coherence between prefrontal and parietal areas
358 also reflects the content of WM[67-69]. For a more complete review of findings of inter-areal coherence
359 during WM and their relationship to performance, see [70]. The significance of enhancing the efficacy of
360 signals by generating a coherent signal has previously been presented in the context of communication
361 through coherence (CTC)[71-74], as has the idea that phase in the receiving area can influence sensitivity to
362 incoming signals[75,76]. In addition to gating of efficacy by phase of the receiving area (as in CTC, where this
363 gating can make a downstream area more sensitive to input from one source than another[77]), the precise
364 timing of spikes relative to oscillations even within a coherently oscillating site (i.e. phase coding) could

365 also be crucial when this timing is going to be gated back into signal strength using a coherent oscillation
366 in the receiving area.

367 We found that WM signals allow expression of visual representations in the form of a neural phase
368 code, indicating that prefrontal cortex could recruit sensory areas using a WM-induced oscillation. This
369 new finding, along with the abundant evidence of coherent oscillations across brain areas during WM[70],
370 lead to a working hypothesis about how WM can recruit sensory areas. Consistent with sensory
371 recruitment theories of WM[37,78-80], these results suggest that sensory and memory signals could be
372 preserved in sensory areas without being expressed in their average firing rate. This latent information
373 could be expressed in the form of a phase code in response to a WM-induced oscillation, and is
374 potentially readable by other areas that have oscillations coherent with the oscillatory frame of reference
375 induced by WM. This proposed recruitment through coherence framework of working memory offers an
376 explanation for how WM can recruit highly feature-sensitive sensory areas in the absence of robust firing
377 rate changes within them.

378

Materials and methods

Experimental model details

We recorded from two male rhesus monkeys (Macaca mulatta, 12 and 16Kg). All experiments and animal procedures in this study were in accordance with the National Institutes of Health Guide for the Care and Use of Laboratory Animals and the Society for Neuroscience Guidelines and Policies. Protocols for experimental and behavioral procedures were approved by the University of Utah Institutional Animal Care and Use Committee.

General and surgical procedures

All surgeries were performed under aseptic conditions, using standard techniques and gas anesthesia, with appropriate peri-surgical analgesia and monitoring. After the study's conclusion, both animals remained healthy and were subsequently utilized in other research endeavors. Stereotactic surgery coordinates for the PFC and V4 chambers (20mm diameter) were performed for monkey 1, right hemisphere, at (AP 25+(2), ML 15 (±0)) and (AP -5(-1), ML 20+(2)), and for monkey 2, left hemisphere, at (AP 30+(1-2), ML 15-(1-2)) and (AP -5-(1-2), ML 20+(1-2)).

Behavioral tasks

We programmed all behavioral tasks using the NIMH Monkeylogic toolbox (ML2) 55, on 64-bit Matlab software (The MathWorks, Inc., Natick, MA). We monitored eye position with an infrared optical eye-tracking (EyeLink 1000, SR Research, Ottawa, Canada). Visual tasks were presented on a VG248 ASUS LED monitor with a refresh rate of 144 Hz and resolution of 1920 x 1080 pixels.

V4 RF mapping

On a daily basis, we first identified V4 RFs using audible responses to oriented bars. Second, we presented a series of visual stimuli on a black background, to quantitatively estimate V4 RFs based on the neuron's firing rate response. Visual stimuli were white circles (1dva diameter), 100ms on, 100ms off, pseudorandomly presented in a 7x7 grid spaced 2.5 dva between stimuli. The monkeys fixated on a central white circle (1dva diameter) throughout the trial.

409 *FEF RF mapping*

410 We estimated FEF RFs using electrical stimulation within the anterior bank of the arcuate sulcus, in
411 biphasic microcurrent pulses (50µA) using a S88 Grass stimulator. Stimulation was performed via tungsten
412 microelectrodes (FHC, Bowdoin, ME). FEF sites were identified based on the landing point of the evoked
413 eye movement following stimulation with currents ≤50µA.

414

415 *Memory guided saccade tasks*

416 To assess the influence of WM on the representation of sensory stimuli, we used a variant of MGS task
417 with a background stimulus (Fig. 1A). The MGS-background task is similar to classic MGS task with a task-
418 irrelevant full field stimulus in the background. The background stimulus was an oriented grating, which
419 could appear in one of four orientations and 4 contrasts (0% contrast is just a classic MG task). The WM
420 cue was placed either within the overlapping RF of FEF and V4 (IN condition) or 180 degrees away (OUT
421 condition). During FEF inactivation experiments, a classic 8 location MGS task with no background was
422 used to assess the behavioral consequences of drug injection over space and time (Fig. 3B-E), in addition
423 to the MGS-background task to measure information coding.

424

425 ***Neurophysiological recording***

426 We recorded the activity of 145 V4 neurons across 88 recording sessions (55 sessions Monkey E, 33
427 sessions Monkey O), including 66 V4 neurons during 33 FEF inactivation sessions (29 sessions Monkey E, 4
428 sessions Monkey O). We recorded neurophysiological activity using Neuralynx and Blackrock data
429 acquisition systems. We digitized spike waveforms at 32 KHz, and performed offline spike sorting
430 manually. We used single tungsten microelectrodes of 200µm diameter, with epoxylite insulation (FHC,
431 Bowdoin, ME), and linear 16-channel arrays (Plexon, Dallas, TX). Electrodes were inserted using a
432 hydraulic microdrive (Narishige, Japan).

433 *V4 recordings:* We simultaneously recorded from FEF (single electrode) and V4 (single or linear array
434 electrodes). In this paper we only present the data from the V4 recordings.

435 *FEF inactivation with V4 recording:* FEF was pharmacologically inactivated through infusion of 0.5-1µL of
436 the GABA-a agonist muscimol, using a custom microinjectrode system (described in [81,82]). Muscimol
437 concentration was 5mg/ml (pH 6.5 to 7). V4 activity was recorded from a site with RFs overlapping the

438 estimated FEF RF, before and after FEF inactivation. Performance on the memory guided saccade task was
439 used to verify FEF inactivation.

440

441 ***Data analysis***

442 *Quantification and statistical analysis*

443 For all analyses of V4 responses (main Figs. 1,2,4), we pooled V4 data from simultaneous FEF-V4 recording
444 sessions with data from FEF inactivation sessions (using the V4 data prior to FEF inactivation). For the
445 results of Figure 3, we assess the role of FEF on V4 coding using inactivation data in which we recorded
446 from V4 before and after FEF inactivation. Evaluations of neural responses to background stimuli of
447 varying contrast or orientation include the three non-zero contrast values. Wherever a statistical test is
448 not specified it is Wilcoxon sign rank. P values are reported up to three decimal digits, and p values less
449 than 0.001 are reported as $p<10^{-x}$. The β range is defined as 14-22 Hz. The significance of the histograms
450 was indicated using asterisks (* for $p < 0.05$, ** for $p < 0.01$, and *** for $p < 0.001$), while non-significant
451 results were denoted with 'ns' (not significant, $p > 0.05$).

452 *Behavioral analyses*

453 The percentage of correct was defined as correctly completed trials divided by all completed trials (Fig.
454 3C). Target window size (used for % correct calculations and for rewarding the animal) was a circle of
455 radius 2 dva for cue eccentricities <7 dva, and radius 4 dva for eccentricities >7 dva.

456 Reaction time (RT) was the time between cue and saccade onset. Saccade error was defined as the
457 difference between the endpoint of the saccade and the cue location. For across-session behavioral
458 analysis (Fig. 3D-E), RT and error were normalized within each session by dividing by the median RT/error
459 of all before inactivation trials.

460 *LFP power spectrum, spike-phase locking, and STA*

461 The power spectral density of the local field potentials (LFPs) was calculated using the multitaper method,
462 employing three tapers (discrete prolate spheroidal (DPSS)-Slepian sequences) for each trial and channel.
463 For population LFP power statistics, LFP power spectrums were normalized, [(X-min)/(max-min)]. In
464 sessions with array recordings (51/88 sessions) power calculations were performed for each channel and
465 then averaged across all channels in that session before calculating population statistics. To quantify the
466 reliability of spike timing relative to the LFP of the same channel, we employed the Spike-phase locking
467 (SPL) method [83], which measures the consistency or locking strength of spike phases to the LFPs. This is

468 achieved by calculating the angular summation between phases of LFPs and spike times. The amplitude of
469 the SPL indicates the strength of spike locking to LFP phase, while the angle reflects the phases of LFPs
470 when spikes occurred. For the spike-triggered average (STA) of the LFP, we first normalized the LFP by
471 taking the z-score of the LFP across timepoints within 100ms of a spike for each trial, then averaged those
472 values across trials. We concentrated on neurons with well-defined STAs. Low contrast STAs lacked a clear
473 peak and were excluded from the analysis.

474

475 *Rate and phase coding capacity*

476 Our primary means of measuring coding capacity was the method developed by Panzeri and colleagues,
477 which allowed us to quantify and compare information contained in rate and phase codes [84,85]. This
478 calculation of coding capacity was done in four steps. 1) First, using the FIR filter, LFPs were filtered into
479 ten different frequency bands (1-4; 4-8; 8-12; 12-17; 17-22; 22-27; 27-35; 35-55; 65-90; 90-120). 2) Next,
480 based on Hilbert transform, the phase of filtered LFPs were extracted. 3) Subsequently, the average of
481 phases at the time of spike occurrence were estimated for a window of 100ms duration with 100ms shift.
482 4) Finally, mutual information (MI) was calculated between these average phases (phase code) or average
483 spike rate (rate code) and different stimuli. The MI was calculated across all stimulus contrasts and
484 orientations. For full mathematical details see [84]. The configuration we used was: direct method, biased
485 naive estimates and 20 bootstraps [85].

486

487 ***Mathematical modelling methods***

488 Details of this model were previously published in *Frontiers in Computational Neuroscience* [86].

489 *Neural field model*

490 Our neural field model is defined by be a periodic orientation tuning domain parameter $\theta \in$
491 $[0, \pi)$. This neural field model is intended to represent a hypercolumn-like population with a subset of
492 cells within the neural field preferentially responsive to a θ-oriented stimulus. This model has been
493 studied in detail in a previous article by our group [86]. The neural field model is described by $u(\theta, t)$,
494 $v(\theta, t)$, the e- and i-activity for every θ-location on the ring, that solves the integro-differential equation:

$$\tau_e \frac{\partial u}{\partial t} = -u + f_\sigma(W * [w_{ee}u - w_{ei}v] + I_e),$$
$$\tau_i \frac{\partial v}{\partial t} = -v + f_\sigma(W * [w_{ie}u - w_{ii}v] + I_i),$$

The integral convolution "*" in the above, is over the θ-domain, with $W(\theta)$ being the von-Mises periodic weight kernel

$$W(\theta) = \frac{1}{\pi I_0(\kappa)} exp\ (\kappa cos\ (2\theta)\ )\ .$$

A mass-model at θ and θ' will be connected with weight $W(\theta - \theta')d\theta'$. The parameter κ is the inverse-variance-like scale parameter that shapes the broadness/tightness of the distribution, and $I_0(\kappa)$ is the order-zero modified Bessel function of the first kind, which serves as the normalization constant. Note that the half-circle orientation tuning domain $\theta \in\ [0, \pi)$ necessitates a "2" factor in the weight function to be π-periodic. The same spatial scale κ is used for both e- and i-cell populations.

The $f_\sigma(I)$ function defines the output firing rate of each population as a function of its input I---an F-I curve. We have used a sigmoidal-shaped F-I curve defined as the inverse mean first passage time, plus a 5ms refractory period, of a leaky integrate an fire LIF model neuron driven by uncorrelated Gaussian white noise $\sigma\xi(t)$ with standard deviation σ (see for example [86,87]:

$$C\frac{dV}{dt} = g_l(V_l - V) + I +\ \sigma\xi(t),$$

with capacitance $C = 1$ micro-Farads, spike threshold voltage $V_t =\ -50$mV, and reset and leak voltages $V_r = V_l =\ -65$mV (all parameters are listed in Table S1). With these parameters, $I = 1$nA of current induces the membrane voltage to approach spike threshold in the absence of noise. Increasing noise parameter σ has the effect of reducing the overall gain of the F-I curve (see [86], for more details on this model).

Three types of external inputs were given to the neural field: working memory inputs, stimulus inputs, and random inputs. WM inputs are uniform current inputs, added to I_e and I_i, over the entire neural field (equal for all θ-values). These uniform inputs raised very slightly the mean firing rate and oscillation frequency and represent an WM-like or attentional-like enhancement of hypercolumn activity. Stimulus inputs are orientation-tuned given by Von Mises-like distribution functions

$$S(\theta)\ =\ e^{\kappa_s cos\ (2(\theta-\theta_0))-\kappa_s}$$

in which the peak strength (set to unity) of the stimulus located at orientation θ_0. We fix $\theta_0\ = \pi/2$--a 90-degree (vertical) orientated stimulus, without loss of generality. Finally, to capture the temporal variations in network oscillations observed in real cortical tissues, on simulations in which we assessed sensory coding (see below), we included slow-timescale Ornstein-Ulenbeck noise $y(t)$ to both e- and i-cell input currents I_e and I_i globally to the entire network (uniformly across all θ-values). The dynamics of y are given by the stochastic differential equation

$$\tau_z \frac{dy}{dt} = -y + \sigma_z \sqrt{\tau_z}\, \xi(t),$$

where $\xi(t)$ is uncorrelated zero-mean unit-variance gaussian white noise. This equation results in a normal stationary distribution of y-values, with zero-mean, and standard deviation σ_z, and a temporal autocorrelation decay timescale $\tau_z = 50$ms, so that the network oscillations, which were typically in the 20 Hz range (50 ms oscillation cycles), showed robust cycle to cycle variability but little long-timescale multi-cycle correlation.

In the absence of any external input, we set neural field model to be very near the a supercritical Hopf instability (see [86]) in which additional current above a current threshold I^*, elicited oscillations with amplitude emerging continuously from zero, and oscillation frequency in the β-band around 18-20 Hz. From this I^* parameter starting point we ran simulations from over four levels of WM input (uniform current) and four levels of orientation-selective stimulus input (contrast levels), starting from zero. We call these WM 0,1,2,3 levels, and contrast levels 0,1,2,3. Altogether, the input to cells can be represented by

$$I_e(\theta, t) = I_{e0} + a\, \Delta_{stim} S(\theta) + b\, \Delta_{WM} + y(t),$$
$$I_i(\theta, t) = I_{i0} + a\, \Delta_{stim} S(\theta) + b\, \Delta_{WM} + y(t),$$

where Δ_{stim} and Δ_{WM} are the current increments for the respective input levels of stimulus $a = 0,1,2,3$ and WM $b = 0,1,2,3$. In addition to the input current changes that occur for our model, it is common to accept that increased stimulus input comes with increased input current fluctuations. We modeled this by adjusting the σ -parameter the F-I curve as a function of contrast input:

$$\sigma = \sigma_0 + a\Delta_\sigma.$$

Coding performance

The phase- and rate-based responses of the neural field model can be used to discriminate the input stimuli. We have chosen to discriminate the neural field model responses at the neural field locations $\theta = \pi/2$ and $\pi/4$. We computed the coding performance for two competing codes: a rate code (i.e., a spike count code) and a phase code. To define the phase variable in the phase code, we examined the proxy LFP signal formed by averaging e-cell rate responses over the entire field domain. We derived a phase angle $\varphi(t) \in [-\pi, \pi]$ of oscillation via the Hilbert transform of this LFP signal. After segmenting the simulation run time into oscillation cycles $\varphi(t) \in [-\pi, \pi]$, for $t \in [0, T]$, where $T = 1/f$ is oscillation period. The mean rate response is simply $\lambda_\theta = \frac{1}{T}\int_0^T u(\theta, t)dt$, from which we assume Poisson-distributed n number of spikes are emitted:

$$p_\theta(n) = \frac{(\lambda_\theta T)^n e^{-\lambda_\theta T}}{n!},$$

which constituted the rate code distribution.

The phase code distribution is obtained from the rate response $u(\theta, t)$, by using a change-of-variables between time and phase $t = g(\varphi)$, where $g(\varphi)$ is the inverse of the Hilbert phase angle:

$$q_\theta(\varphi) = \frac{1}{\lambda_\theta T}\, u\big(\theta, g(\varphi)\big) g'(\varphi).$$

Using the spike count and phase distributions as the basis of the rate and phase codes, respectively, we computed two different measures of coding performance. First, to measure the amount of information gained from the code at $\theta = \pi/2$, given one assumes the data are distributed according to $\theta = \pi/4$, we computed the information gain rate (IG)--the Kullback Libler divergence (in natural units of information, nats):

$$IG_\varphi = D_{KL}\left(q_{\frac{\pi}{4}} \,||\, q_{\frac{\pi}{2}}\right),$$
$$IG_n = D_{KL}\left(p_{\frac{\pi}{4}} \,||\, p_{\frac{\pi}{2}}\right),$$

where $D_{KL}(p||q) = \int p \, ln \, ln \left(\frac{p}{q}\right) dx$. Second, we computed the mutual information (MI) between stimulus feature $\theta = \pi/2$ or $\pi/4$, and the phase data φ. We assumed the two stimuli were equally likely on a given ``trial" in which case the probability of each stimulus was 1/2. The phase mutual information MI_φ is then defined as the Kullback Libler divergence D_{KL} (using log-base-two, in this case) between the pooled distributions $\frac{1}{2} q_{\pi/2} + \frac{1}{2} q_{\pi/4}$ to the product distribution $q_{\pi/2} q_{\pi/4}$; and similarly, for the rate codes:

$$MI_\varphi = D_{KL}\left(\frac{1}{2} q_{\frac{\pi}{2}} + \frac{1}{2} q_{\frac{\pi}{4}} \,||\, q_{\frac{\pi}{2}} q_{\frac{\pi}{4}}\right),$$
$$MI_n = D_{KL}\left(\frac{1}{2} p_{\frac{\pi}{2}} + \frac{1}{2} p_{\frac{\pi}{4}} \,||\, p_{\frac{\pi}{2}} p_{\frac{\pi}{4}}\right).$$

Data availability

The code for mathematical modelling are publicly available at https://osf.io/dhcr2/. The full dataset is publicly available at https://gin.g-node.org/KClark/Parto_eLife_2024 (doi: 10.12751/g-node.6icjl8). Further information for data and resources should be directed to Lead Contact, Behrad Noudoost (behrad.noudoost@utah.edu).

Acknowledgements

This work was supported by NIH grants EY026924 & NS113073 to B.N, and an Unrestricted Grant from Research to Prevent Blindness, New York, NY, to the Department of Ophthalmology & Visual Sciences, University of Utah.

Author contributions

Conceptualization, M.P., I.V., and B.N.; methodology, I.V., K.C., and B.N.; software, M.P., M.Z.; formal analysis, M.P. and M.Z., B.N.; modeling: W.N.; writing – original draft, M.P. and M.Z., K.C., B.N.; writing – review & editing, all authors; visualization, M.P., W.N., K.C.; supervision, B.N.; funding acquisition, B.N.

Declaration of interests

The authors declare no competing interests.

Supplemental information

Document S1. Figures S1-S16 and Table S1.

581 ## Figure legends

582 **Figure 1. WM alters β oscillatory power but not firing rates in V4.**

583 A) Memory-guided saccade with background (MGS-background) task. The monkey fixated and a
584 peripheral visual cue appeared (Cue). The monkey maintained fixation while remembering the cue
585 location (~1s; Delay), and after the fixation point disappeared, executed a saccadic eye movement to the
586 remembered location (Response) to receive a reward. Throughout the task, there was a task-irrelevant,
587 full-field oriented bar background; the background contrast ranged from 0-64%, in one of 4 orientations.
588 The memory location was either inside the extrastriate RF (IN condition, shown) or 180 degrees away
589 (OUT condition). Neurophysiological recordings of spiking and LFP activity were made from extrastriate
590 visual area V4, with linear array or single electrodes.

591 B-C) Mean firing rate of a sample neuron over time for three different contrasts (B) or orientations (C) of
592 the background stimulus, for the IN (left) and OUT (right) conditions. Shaded areas in all panels show
593 standard error of mean (SEM).

594 D-E) Mean firing rate of the population of 145 neurons over time for three different contrasts (low,
595 medium, and high contrast, D) and four different orientations (preferred, nonpreferred, and middle 1 & 2
596 orientations, E) for the IN condition (left) and OUT (right) conditions.

597 F) Time course of mean F-statistic values across 145 neurons, based on a one-way ANOVA for
598 discrimination between 12 stimulus conditions for the IN (red) and OUT (black) conditions.

599 G) Scatter plot of F-statistic averaged in the last 700ms of the delay period for each session, for the IN vs.
600 OUT conditions. Histogram in the upper right shows the distribution of change in F-statistic (OUT-IN)
601 across sessions.

602 H) Mean power spectrum of the LFP recorded from the same channel as the sample V4 neuron in (B),
603 during the delay period for the IN (red) vs. OUT (black) conditions. Inset panel shows 8-25 Hz. Asterisk
604 indicates a significant difference ($p<0.05$) in the range shown.

605 I) Mean power spectrum of population of the V4 LFPs (88 sessions) during the delay period for the IN (red)
606 vs. OUT (black) conditions. Inset shows the power spectrum between 14-22 Hz.

607 J) Scatter plot of power spectrum averaged in the β range for each session, for the IN vs. OUT conditions.
608 Histogram in the upper right shows the distribution of change in power (OUT-IN) across sessions (***, p
609 <0.001).

610

611 **Figure 2. WM alters the sensory representation in extrastriate cortex.**

612 A) The distribution of spikes generated by a sample V4 neuron across various phases of β oscillations
613 during the delay period. Arrows show the average of phase distributions for the IN (red) and OUT (black)
614 conditions.

615 B) Scatter plot of SPL in the β range for each neuron, for the IN vs. OUT conditions. Histogram in the upper
616 right shows the distribution of change in SPL (OUT-IN) across neurons. Red cross indicates population
617 mean. Green dot shows the selected sample neuron in A.

618 C) Spike-triggered average of the normalized LFP of a sample neuron during the delay period, for the high
619 contrast (red) and low contrast (blue) background stimuli, for the IN (left) and OUT (right) conditions.
620 Shaded bars indicate the slopes in the falling phase.

621 D) Histogram of the distribution of STA slopes (abs $(V_{peak} - V_{trough})/(time_{peak} - time_{trough})$) across neurons,
622 for high contrast (red) and low contrast (blue) stimuli, for the IN (left) and OUT (right) conditions.

623 E) Population phase (left) and rate (right) coding over time, for the IN (red) and OUT (black) conditions,
624 based on mutual information (MI) between 12 stimulus conditions. MI was measured in 100ms windows
625 with steps of 100ms. Shaded areas show standard error of mean (SEM).

626 F) Scatter plot of MI using a phase code in the β range (left) and rate code (right) for each neuron, for the
627 IN vs. OUT conditions. Red crosses indicate population mean. Histograms in the upper right show the
628 distribution of differences in MI (IN-OUT) across neurons.

629 G) Phase coding, measured by MI (colorbar), as a function of frequency and time, for memory IN (left) and
630 OUT (right). Black rectangle shows the time and frequency range selected for phase code analysis. (*, p
631 <0.05; **, $p<0.01$; ***, $p<0.001$; ns, $p>0.05$)

632

633 **Figure 3. FEF inactivation alters WM behavioral performance and phase coding in visual areas.**

634 A) V4 recordings were made before and after infusion of muscimol into FEF. Muscimol injections into FEF
635 were made with a custom microinjectrode, at sites with stimulation-evoked saccade endpoints
636 overlapping with simultaneous V4 recording site RFs.

637 B) Eye traces for 8 MGS target locations, before (left) and after (right) FEF inactivation, for an example
638 session where 0.5 microliter of muscimol was injected into the FEF; performance deficits were localized to
639 the infusion hemifield.

640 C) Average behavioral performance across sessions, at different locations over time following FEF
641 inactivation (red pre-inactivation; green, blue, and black, 1, 2, and 3 hours after inactivation, respectively).
642 Data from each session is aligned so that 0 degrees corresponds to the FEF RF.

643 D-E) Normalized saccade error (D) and reaction times (E) for the memory IN (red) and OUT (black)
644 conditions, over time relative to the FEF inactivation. Black bar indicates times with a significant
645 difference between IN and OUT. Shaded areas show SEM across sessions.

646 F) Heatmap shows phase coding (MI, colorbar) over time and frequency for 66 V4 neurons, for the IN
647 condition, before (left) and after (right) FEF inactivation. Black rectangle indicates time and frequency
648 range considered in (G-H): 14-22Hz, 200-800ms after start of delay period.

649 G) Strength of β phase coding over time, for memory IN, before (red) and after inactivation (blue). The
650 phase-code MI is averaged in the β range. Shading shows SEM across neurons. Gray area indicates time
651 window plotted in (H).

652 H) Scatter plot of β phase MI during the delay period (shaded area in G) of the IN condition for each V4
653 neuron, before vs. after FEF inactivation. Red square shows population mean. The histogram in the upper
654 right shows the distribution of difference in MI (Pre-Post) across neurons. (*, $p < 0.05$; **, $p < 0.01$; ***, p
655 < 0.001; ns, $p > 0.05$)

656

657 **Figure 4. Experimental and computational dependence of firing rate, phase-coded information, and**
658 **rate-coded information on changes in peak oscillation frequency.**

659 A) Schematic of dynamical neural field network architecture. Excitatory and inhibitory units are
660 interconnected and organized to respond to different input stimuli (theta). Units also receive a global WM
661 input (not shown); see Methods for description of connectivity weights.

662 B) Example activity of excitatory units in the model over time, in response to an input at π/2. Excitatory
663 units are plotted along the y-axis according to their input tuning, which ranges from 0 to π. Activity
664 reflects both a beta-frequency oscillation across the entire population, and an earlier and stronger
665 response of units whose preference matches the input feature (i.e., phase and rate coding).

C) Information about the input stimulus feature coded by phase and rate (left and right y-axes; see Methods) in the neural field model, as a function of WM input strength.

D) Phase information (shades of orange) and rate information (shades of blue) as a function of contrast levels and oscillation frequency, for the neural field model. Data for each contrast is divided into deciles based on oscillation frequency, variability in which comes from noise in the WM input strength. Note that rate code values are several orders of magnitude smaller than phase code values (left vs. right y-axis). Error bars show standard deviation.

E) Correlation between oscillation frequency and firing rate in the neural field model under conditions of noisy WM input strength.

F) Relationship between frequency of peak LFP power and firing rate during the delay period for the memory IN (red) and OUT (black) conditions, for two example neurons with increased (left) or decreased (right) firing rate during the IN condition. Each dot shows the average frequency of max power and normalized firing rate for a subsample consisting of 50% of trials (n=100 subsamples per neuron).

G) Average normalized response as a function of peak frequency, pooled across subsamples of trials from each of 145 V4 neurons (100 subsamples/neuron), during the IN (red) and OUT (blue) conditions, during the delay period (left) and the cue period (right). Plot shows mean±SE for all subsamples with the peak frequency indicated on the x-axis.

References

1 Squire, R. F., Noudoost, B., Schafer, R. J. & Moore, T. Prefrontal Contributions to Visual Selective Attention. *Annual Review of Neuroscience* **36**, 451–466, doi:10.1146/annurev-neuro-062111-150439 (2013).

2 Miller, E. K. & Cohen, J. D. An integrative theory of prefrontal cortex function. *Annual review of neuroscience* **24**, 167–202, doi:10.1146/annurev.neuro.24.1.167 (2001).

3 Miller, B. T. & D'Esposito, M. Searching for "the top" in top-down control. *Neuron* **48**, 535–538 (2005).

4 Paneri, S. & Gregoriou, G. G. Top-Down Control of Visual Attention by the Prefrontal Cortex. Functional Specialization and Long-Range Interactions. *Frontiers in Neuroscience* **11**, 545, doi:10.3389/fnins.2017.00545 (2017).

5 Gazzaley, A. & Nobre, A. C. Top-down modulation: bridging selective attention and working memory. *Trends in Cognitive Sciences* **16**, 129–135, doi:10.1016/j.tics.2011.11.014 (2012).

6 Knight, R. T., Grabowecky, M. F. & Scabini, D. Role of human prefrontal cortex in attention control. *Advances in neurology* **66**, 21–34; discussion 34–26 (1995).

7 Johnson, E. L. *et al.* Bidirectional Frontoparietal Oscillatory Systems Support Working Memory. *Current biology : CB* **27**, 1829-1835.e1824, doi:10.1016/j.cub.2017.05.046 (2017).

8 Merrikhi, Y. *et al.* Spatial working memory alters the efficacy of input to visual cortex. *Nature communications* **8**, 15041, doi:10.1038/ncomms15041 (2017).

9 Bahmani, Z., Daliri, M. R., Merrikhi, Y., Clark, K. & Noudoost, B. Working Memory Enhances Cortical Representations via Spatially Specific Coordination of Spike Times. *Neuron* **97**, 967–979.e966, doi:10.1016/j.neuron.2018.01.012 (2018).

10 Noudoost, B., Clark, K. L. & Moore, T. Working memory gates visual input to primate prefrontal neurons. *eLife* **10**, e64814, doi:10.7554/eLife.64814 (2021).

11 Chelazzi, L., Duncan, J., Miller, E. K. & Desimone, R. Responses of neurons in inferior temporal cortex during memory-guided visual search. *Journal of neurophysiology* **80**, 2918–2940 (1998).

12 Mendoza-Halliday, D., Torres, S. & Martinez-Trujillo, J. C. Sharp emergence of feature-selective sustained activity along the dorsal visual pathway. *Nature neuroscience* **17**, 1255–1262, doi:10.1038/nn.3785 (2014).

13 Leavitt, M. L., Mendoza-Halliday, D. & Martinez-Trujillo, J. C. Sustained Activity Encoding Working Memories: Not Fully Distributed. *Trends in Neurosciences* **40**, 328–346, doi:10.1016/j.tins.2017.04.004 (2017).

14 Chelazzi, L., Miller, E. K., Duncan, J. & Desimone, R. Responses of neurons in macaque area V4 during memory-guided visual search. *Cerebral cortex (New York, N.Y. : 1991)* **11**, 761–772 (2001).

15 Zaksas, D. & Pasternak, T. Directional signals in the prefrontal cortex and in area MT during a working memory for visual motion task. *The Journal of neuroscience* **26**, 11726–11742, doi:10.1523/JNEUROSCI.3420-06.2006 (2006).

16 Soto, D., Wriglesworth, A., Bahrami-Balani, A. & Humphreys, G. W. Working memory enhances visual perception: Evidence from signal detection analysis. *Journal of Experimental Psychology: Learning, Memory, and Cognition* **36**, 441–456, doi:10.1037/a0018686 (2010).

17 Pan, Y. & Zhang, X. Visual working memory enhances target discrimination accuracy with single-item displays. *Attention, Perception & Psychophysics* **82**, 3005-3012, doi:10.3758/s13414-020-02041-y (2020).

18 Hallenbeck, G. E., Sprague, T. C., Rahmati, M., Sreenivasan, K. K. & Curtis, C. E. Working memory representations in visual cortex mediate distraction effects. *Nature Communications* **12**, 4714, doi:10.1038/s41467-021-24973-1 (2021).

19 Hollingworth, A. & Luck, S. J. The role of visual working memory (VWM) in the control of gaze during visual search. *Attention, perception & psychophysics* **71**, 936–949, doi:10.3758/APP.71.4.936 (2009).

20 Hollingworth, A., Matsukura, M. & Luck, S. J. Visual working memory modulates rapid eye movements to simple onset targets. *Psychological science* **24**, 790–796, doi:10.1177/0956797612459767 (2013).

21 Pan, Y., Lin, B., Zhao, Y. & Soto, D. Working memory biasing of visual perception without awareness. *Attention, Perception & Psychophysics* **76**, 2051-2062, doi:10.3758/s13414-013-0566-2 (2014).

22 Salahub, C. M. & Emrich, S. M. Tuning perception: Visual working memory biases the quality of visual awareness. *Psychonomic Bulletin & Review* **23**, 1854-1859, doi:10.3758/s13423-016-1064-z (2016).

23 Logothetis, N. K., Pauls, J., Augath, M., Trinath, T. & Oeltermann, A. Neurophysiological investigation of the basis of the fMRI signal. *Nature* **412**, 150–157, doi:10.1038/35084005 (2001).

24 Buzsáki, G., Anastassiou, C. A. & Koch, C. The origin of extracellular fields and currents--EEG, ECoG, LFP and spikes. *Nature Reviews. Neuroscience* **13**, 407-420, doi:10.1038/nrn3241 (2012).

25 Einevoll, G. T., Kayser, C., Logothetis, N. K. & Panzeri, S. Modelling and analysis of local field potentials for studying the function of cortical circuits. *Nature Reviews Neuroscience* **14**, 770–785, doi:10.1038/nrn3599 (2013).

26 Herreras, O. Local Field Potentials: Myths and Misunderstandings. *Frontiers in Neural Circuits* **10**, 101, doi:10.3389/fncir.2016.00101 (2016).

27 McCormick, D. A., Connors, B. W., Lighthall, J. W. & Prince, D. A. Comparative electrophysiology of pyramidal and sparsely spiny stellate neurons of the neocortex. *Journal of neurophysiology* **54**, 782–806, doi:10.1152/jn.1985.54.4.782 (1985).

28 Markov, N. T. *et al.* Anatomy of hierarchy: feedforward and feedback pathways in macaque visual cortex. *The Journal of comparative neurology* **522**, 225-259, doi:10.1002/cne.23458 (2014).

29 Pouget, P. *et al.* Visual and motor connectivity and the distribution of calcium-binding proteins in macaque frontal eye field: implications for saccade target selection. *Front Neuroanat* **3**, 2, doi:10.3389/neuro.05.002.2009 (2009).

30 Barone, P., Batardiere, A., Knoblauch, K. & Kennedy, H. Laminar distribution of neurons in extrastriate areas projecting to visual areas V1 and V4 correlates with the hierarchical rank and indicates the operation of a distance rule. *The Journal of neuroscience : the official journal of the Society for Neuroscience* **20**, 3263-3281 (2000).

31 Sommer, M. A. & Tehovnik, E. J. Reversible inactivation of macaque frontal eye field. *Experimental brain research.* **116**, 229–249 (1997).

32 Dias, E. C. & Segraves, M. A. Muscimol-induced inactivation of monkey frontal eye field: effects on visually and memory-guided saccades. *Journal of neurophysiology* **81**, 2191–2214 (1999).

33 Fuster, J. M. Inferotemporal units in selective visual attention and short-term memory. *Journal of Neurophysiology* **64**, 681-697, doi:10.1152/jn.1990.64.3.681 (1990).

34 Supèr, H., Spekreijse, H. & Lamme, V. A. F. A neural correlate of working memory in the monkey primary visual cortex. *Science* **293**, 120–124, doi:10.1126/science.1060496 (2001).

35 Hayden, B. Y. & Gallant, J. L. Working memory and decision processes in visual area v4. *Front Neurosci* **7**, 18, doi:10.3389/fnins.2013.00018 (2013).

36 Anderson, J. C., Kennedy, H. & Martin, K. A. C. Pathways of attention: synaptic relationships of frontal eye field to V4, lateral intraparietal cortex, and area 46 in macaque monkey. *The Journal of neuroscience : the official journal of the Society for Neuroscience* **31**, 10872–10881, doi:10.1523/JNEUROSCI.0622-11.2011 (2011).

37 Lara, A. H. & Wallis, J. D. The Role of Prefrontal Cortex in Working Memory: A Mini Review. *Frontiers in Systems Neuroscience* **9**, 173, doi:10.3389/fnsys.2015.00173 (2015).

38 Zanto, T. P., Rubens, M. T., Thangavel, A. & Gazzaley, A. Causal role of the prefrontal cortex in top-down modulation of visual processing and working memory. *Nature Neuroscience* **14**, 656–661, doi:10.1038/nn.2773 (2011).

39 Awh, E. & Jonides, J. Overlapping mechanisms of attention and spatial working memory. *Trends in cognitive sciences* **5**, 119-126, doi:10.1016/s1364-6613(00)01593-x (2001).

40 Zhou, Y., Curtis, C. E., Sreenivasan, K. K. & Fougnie, D. Common Neural Mechanisms Control Attention and Working Memory. *The Journal of neuroscience : the official journal of the Society for Neuroscience* **42**, 7110-7120, doi:10.1523/JNEUROSCI.0443-22.2022 (2022).

41 Awh, E., Armstrong, K. M. & Moore, T. Visual and oculomotor selection: links, causes and implications for spatial attention. *Trends in cognitive sciences* **10**, 124-130, doi:10.1016/j.tics.2006.01.001 (2006).

42 Gazzaley, A. & Nobre, A. C. Top-down modulation: bridging selective attention and working memory. *Trends in cognitive sciences* **16**, 129-135, doi:10.1016/j.tics.2011.11.014 (2012).

43 Postle, B. R. Working memory as an emergent property of the mind and brain. *Neuroscience* **139**, 23-38, doi:10.1016/j.neuroscience.2005.06.005 (2006).

44 Chun, M. M. Visual working memory as visual attention sustained internally over time. *Neuropsychologia* **49**, 1407-1409, doi:10.1016/j.neuropsychologia.2011.01.029 (2011).

45 Soto, D., Hodsoll, J., Rotshtein, P. & Humphreys, G. W. Automatic guidance of attention from working memory. *Trends in cognitive sciences* **12**, 342-348, doi:10.1016/j.tics.2008.05.007 (2008).

46 Soto, D., Wriglesworth, A., Bahrami-Balani, A. & Humphreys, G. W. Working memory enhances visual perception: evidence from signal detection analysis. *J Exp Psychol Learn Mem Cogn* **36**, 441-456, doi:10.1037/a0018686 (2010).

47 Teng, C. & Kravitz, D. J. Visual working memory directly alters perception. *Nature human behaviour* **3**, 827-836, doi:10.1038/s41562-019-0640-4 (2019).

48 Awh, E., Jonides, J. & Reuter-Lorenz, P. A. Rehearsal in spatial working memory. *J Exp Psychol Hum Percept Perform* **24**, 780-790, doi:10.1037//0096-1523.24.3.780 (1998).

49 Womelsdorf, T., Anton-Erxleben, K. & Treue, S. Receptive field shift and shrinkage in macaque middle temporal area through attentional gain modulation. *The Journal of neuroscience : the official journal of the Society for Neuroscience* **28**, 8934–8944, doi:10.1523/JNEUROSCI.4030-07.2008 (2008).

50 Womelsdorf, T., Anton-Erxleben, K., Pieper, F. & Treue, S. Dynamic shifts of visual receptive fields in cortical area MT by spatial attention. *Nature neuroscience* **9**, 1156–1160, doi:10.1038/nn1748 (2006).

51 Moran, J. & Desimone, R. Selective attention gates visual processing in the extrastriate cortex. *Science* **229**, 782–784 (1985).

52 Mitchell, J. F., Sundberg, K. A. & Reynolds, J. H. Differential attention-dependent response modulation across cell classes in macaque visual area V4. *Neuron* **55**, 131–141, doi:10.1016/j.neuron.2007.06.018 (2007).

53 Merrikhi, Y., Clark, K. L. & Noudoost, B. Concurrent influence of top-down and bottom-up inputs on correlated activity of Macaque extrastriate neurons. *Nature Communications* **9**, 5393, doi:https://doi.org/10.1038/s41467-018-07816-4 (2018).

54 Cohen, M. R. & Maunsell, J. H. Attention improves performance primarily by reducing interneuronal correlations. *Nature neuroscience* **12**, 1594–1600, doi:10.1038/nn.2439 (2009).

55 Armstrong, K. M., Chang, M. H. & Moore, T. Selection and maintenance of spatial information by frontal eye field neurons. *The Journal of neuroscience : the official journal of the Society for Neuroscience* **29**, 15621-15629, doi:10.1523/JNEUROSCI.4465-09.2009 (2009).

826 56 Panichello, M. F. & Buschman, T. J. Shared mechanisms underlie the control of working memory
827 and attention. *Nature* **592**, 601-605, doi:10.1038/s41586-021-03390-w (2021).

828 57 Lebedev, M. A., Messinger, A., Kralik, J. D. & Wise, S. P. Representation of attended versus
829 remembered locations in prefrontal cortex. *PLoS biology* **2**, e365,
830 doi:10.1371/journal.pbio.0020365 (2004).

831 58 Messinger, A., Lebedev, M. A., Kralik, J. D. & Wise, S. P. Multitasking of attention and memory
832 functions in the primate prefrontal cortex. *The Journal of neuroscience : the official journal of the*
833 *Society for Neuroscience* **29**, 5640-5653, doi:10.1523/JNEUROSCI.3857-08.2009 (2009).

834 59 Steinmetz, N. A. & Moore, T. Eye movement preparation modulates neuronal responses in area V4
835 when dissociated from attentional demands. *Neuron* **83**, 496-506,
836 doi:10.1016/j.neuron.2014.06.014 (2014).

837 60 Jonikaitis, D. & Moore, T. The interdependence of attention, working memory and gaze control:
838 behavior and neural circuitry. *Curr Opin Psychol* **29**, 126-134, doi:10.1016/j.copsyc.2019.01.012
839 (2019).

840 61 Noudoost, B., Chang, M. H., Steinmetz, N. A. & Moore, T. Top-down control of visual attention.
841 *Current opinion in neurobiology* **20**, 183–190 (2010).

842 62 Snyder, A. C., Yu, B. M. & Smith, M. A. A Stable Population Code for Attention in Prefrontal Cortex
843 Leads a Dynamic Attention Code in Visual Cortex. *Journal of Neuroscience* **41**, 9163-9176,
844 doi:10.1523/JNEUROSCI.0608-21.2021 (2021).

845 63 Kempen, J. v. *et al.* Top-down coordination of local cortical state during selective attention. *Neuron*
846 **109**, 894-904.e898, doi:10.1016/j.neuron.2020.12.013 (2021).

847 64 Fiebelkorn, I. C. & Kastner, S. Spike Timing in the Attention Network Predicts Behavioral Outcome
848 Prior to Target Selection. *Neuron* **109**, 177-188.e174, doi:10.1016/j.neuron.2020.09.039 (2021).

849 65 Rezayat, E. *et al.* Frontotemporal coordination predicts working memory performance and its local
850 neural signatures. *Nature Communications* **12**, 1103, doi:10.1038/s41467-021-21151-1 (2021).

851 66 Liebe, S., Hoerzer, G. M., Logothetis, N. K. & Rainer, G. Theta coupling between V4 and prefrontal
852 cortex predicts visual short-term memory performance. *Nature Neuroscience* **15**, 456–462,
853 doi:10.1038/nn.3038 (2012).

854 67 Antzoulatos, E. G. & Miller, E. K. Synchronous beta rhythms of frontoparietal networks support
855 only behaviorally relevant representations. *eLife* **5**, e17822, doi:10.7554/eLife.17822 (2016).

856 68 Salazar, R. F., Dotson, N. M., Bressler, S. L. & Gray, C. M. Content-specific fronto-parietal
857 synchronization during visual working memory. *Science* **437**, 1097–1101 (2012).

858 69 Dotson, N. M., Salazar, R. F. & Gray, C. M. Frontoparietal correlation dynamics reveal interplay
859 between integration and segregation during visual working memory. *The Journal of Neuroscience:*
860 *The Official Journal of the Society for Neuroscience* **34**, 13600-13613,
861 doi:10.1523/JNEUROSCI.1961-14.2014 (2014).

70 Rezayat, E., Clark, K., Dehaqani, M.-R. A. & Noudoost, B. Dependence of Working Memory on Coordinated Activity Across Brain Areas. *Frontiers in Systems Neuroscience* **15**, 164, doi:10.3389/fnsys.2021.787316 (2022).

71 Fries, P. Rhythms for Cognition: Communication through Coherence. *Neuron* **88**, 220–235, doi:10.1016/j.neuron.2015.09.034 (2015).

72 Bastos, A. M., Vezoli, J. & Fries, P. Communication through coherence with inter-areal delays. *Current Opinion in Neurobiology* **31**, 173–180, doi:10.1016/j.conb.2014.11.001 (2015).

73 Fries, P. A mechanism for cognitive dynamics: neuronal communication through neuronal coherence. *Trends in cognitive sciences* **9**, 474–480, doi:10.1016/j.tics.2005.08.011 (2005).

74 Parto-Dezfouli, M., Vezoli, J., Bosman, C. A. & Fries, P. Enhanced behavioral performance through interareal gamma and beta synchronization. *Cell Rep* **42**, 113249, doi:10.1016/j.celrep.2023.113249 (2023).

75 Cardin, J. A. *et al.* Driving fast-spiking cells induces gamma rhythm and controls sensory responses. *Nature* **459**, 663–667, doi:10.1038/nature08002 (2009).

76 Womelsdorf, T. *et al.* Modulation of neuronal interactions through neuronal synchronization. *Science* **316**, 1609–1612, doi:10.1126/science.1139597 (2007).

77 Bosman, C. A. *et al.* Attentional stimulus selection through selective synchronization between monkey visual areas. *Neuron* **75**, 875–888, doi:10.1016/j.neuron.2012.06.037 (2012).

78 Harrison, S. A. & Tong, F. Decoding reveals the contents of visual working memory in early visual areas. *Nature* **458**, 632–635, doi:10.1038/nature07832 (2009).

79 Pasternak, T. & Greenlee, M. W. Working memory in primate sensory systems. *Nature reviews. Neuroscience* **6**, 97–107, doi:10.1038/nrn1603 (2005).

80 D'Esposito, M. & Postle, B. R. The Cognitive Neuroscience of Working Memory. *Annual Review of Psychology* **66**, 115–142, doi:10.1146/annurev-psych-010814-015031 (2015).

81 Vanegas, M. I., Hubbard, K. R., Esfandyarpour, R. & Noudoost, B. Microinjectrode System for Combined Drug Infusion and Electrophysiology. *Journal of Visualized Experiments: JoVE*, doi:10.3791/60365 (2019).

82 Noudoost, B. & Moore, T. A reliable microinjectrode system for use in behaving monkeys. *Journal of neuroscience methods* **194**, 218–223, doi:10.1016/j.jneumeth.2010.10.009 (2011).

83 Zarei, M., Parto Dezfouli, M., Jahed, M. & Daliri, M. R. Adaptation Modulates Spike-Phase Coupling Tuning Curve in the Rat Primary Auditory Cortex. *Front Syst Neurosci* **14**, 55, doi:10.3389/fnsys.2020.00055 (2020).

84 Kayser, C., Montemurro, M. A., Logothetis, N. K. & Panzeri, S. Spike-phase coding boosts and stabilizes information carried by spatial and temporal spike patterns. *Neuron* **61**, 597–608, doi:10.1016/j.neuron.2009.01.008 (2009).

85 Magri, C., Whittingstall, K., Singh, V., Logothetis, N. K. & Panzeri, S. A toolbox for the fast information analysis of multiple-site LFP, EEG and spike train recordings. *BMC Neurosci* **10**, 81, doi:10.1186/1471-2202-10-81 (2009).

86 Nesse, W. H., Clark, K. L. & Noudoost, B. Information representation in an oscillating neural field model modulated by working memory signals. *Front Comput Neurosci* **17**, 1253234, doi:10.3389/fncom.2023.1253234 (2023).

87 Sanzeni, A., Histed, M. H. & Brunel, N. Response nonlinearities in networks of spiking neurons. *PLoS Comput Biol* **16**, e1008165, doi:10.1371/journal.pcbi.1008165 (2020).

Parto-Dezfouli et al 2024
Figure 1
2 columns

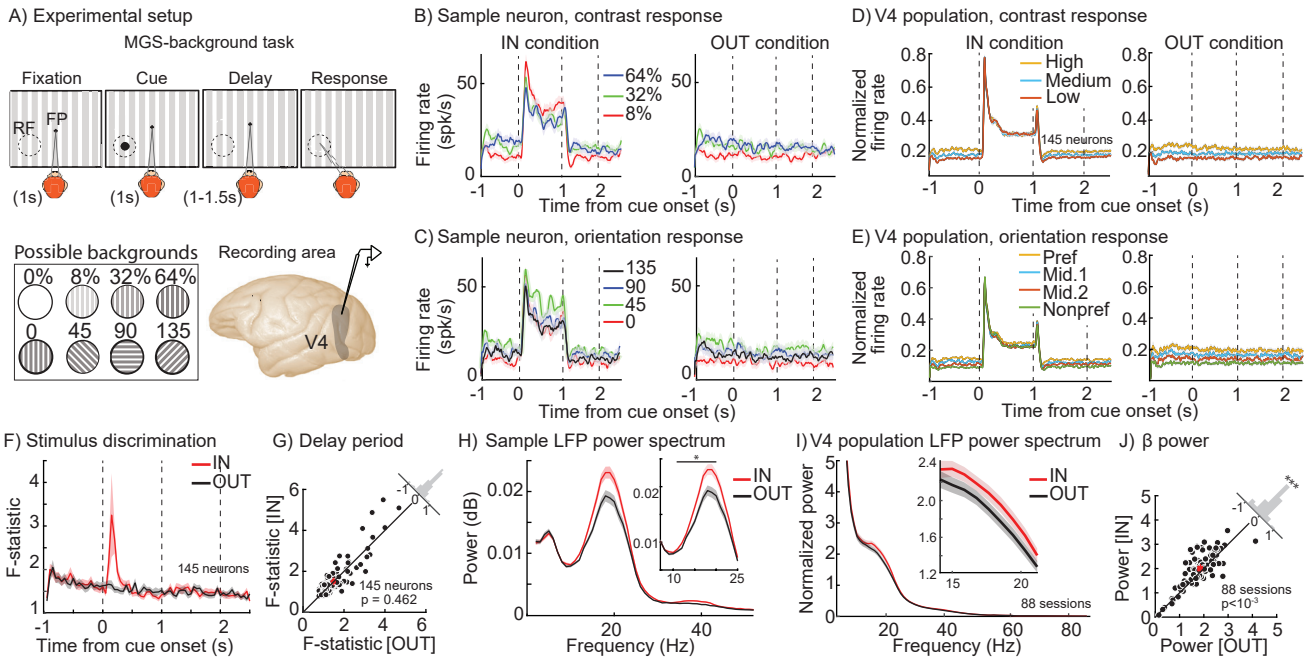

Parto-Dezfouli et al 2024
Figure 2
2 columns

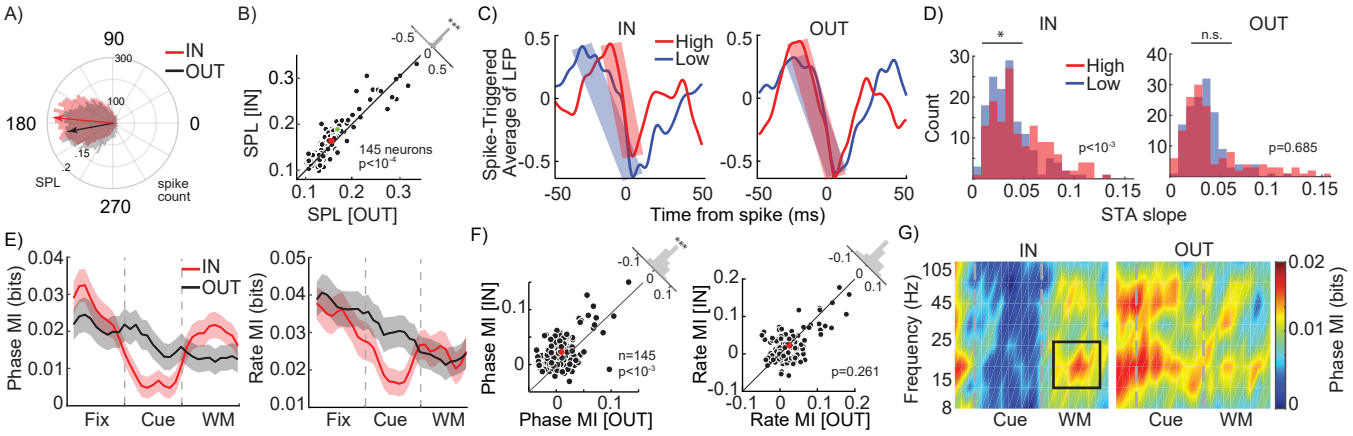

Parto-Dezfouli et al 2024
Figure 3
2 columns

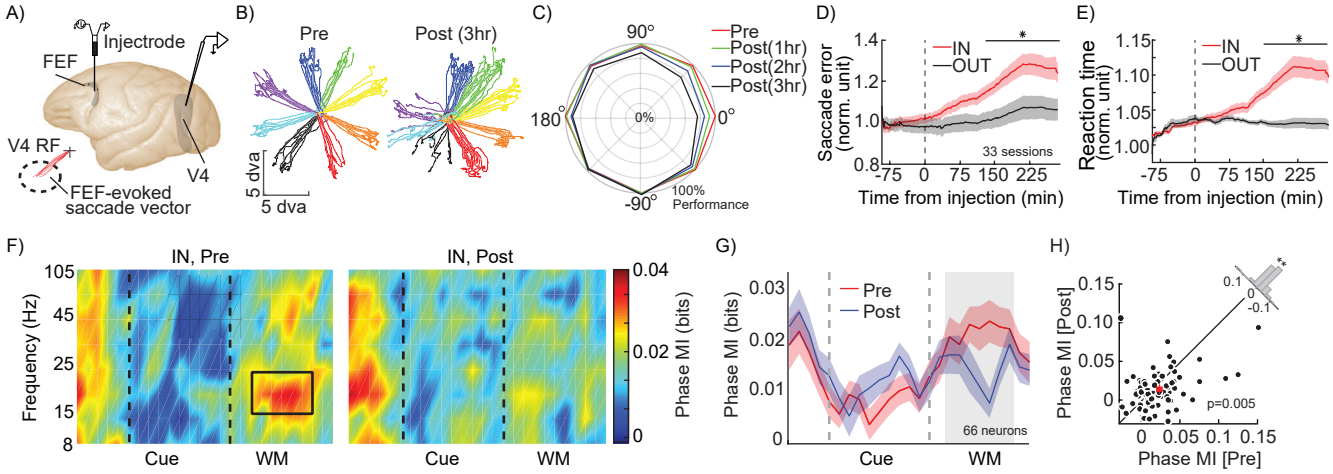
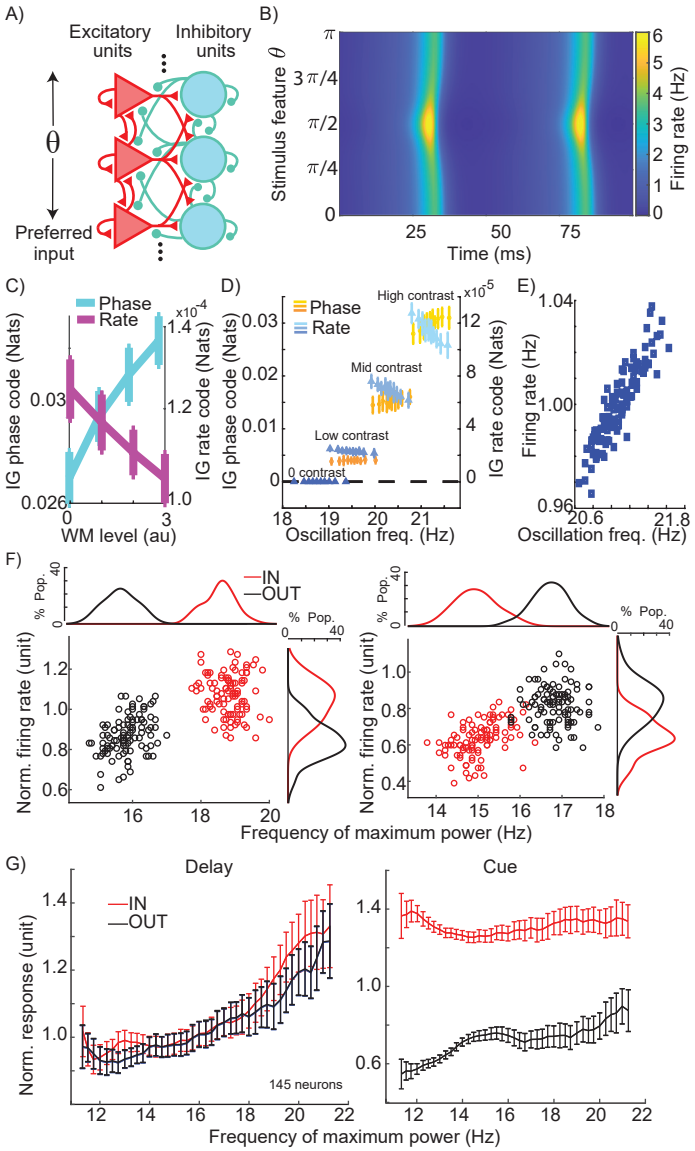
Parto-Dezfouli et al 2024
Figure 4
1 column